Opto-Electronic Science

CN 51-1800/O4 ISSN (Print) 2097-0382 ISSN (Online) 2097-4000

Breaking the speed-resolution trade-off in 3.3-km non-line-of-sight imaging using scanning-free laser reflective tomography

Zewei Wang, Xiaoyin Li, Yinghui Guo*, Hengshuo Guo, Peng Yang, Fei Zhang, Mingbo Pu*, Mingfeng Xu and Xiangang Luo*

Citation: Wang ZW, Li XY, Guo YH et al. Breaking the speed-resolution trade-off in 3.3-km non-line-of-sight imaging using scanning-free laser reflective tomography. *Opto-Electron Sci* **5**, 260007 (2026).

https://doi.org/10.29026/oes.2026.260007

Received: 5 February 2026; Accepted: 21 April 2026; Published online: 9 May 2026

Related articles

Unsupervised learning enabled label-free single-pixel imaging for resilient information transmission through unknown dynamic scattering media

Fujie Li, Haoyu Zhang, Zhilan Lu, et al

Opto-Electronic Advances 2025, **8**(10): 250013 doi: 10.29026/oea.2025.250013

Dual-frequency angular-multiplexed fringe projection profilometry with deep learning: breaking hardware limits for ultra-high-speed 3D imaging

Wenwu Chen, Yifan Liu, Shijie Feng, et al

Opto-Electronic Advances 2025, **8**(9): 250021 doi: 10.29026/oea.2025.250021

Surpassing the diffraction limit in long-range laser engineering via cross-scale vectorial optical field manipulation: perspectives and outlooks

Yinghui Guo, Mingbo Pu, Yang Li, et al

Opto-Electronic Advances 2025, **8**(12): 250256 doi: 10.29026/oea.2025.250256

Optical scanning endoscope via a single multimode optical fiber

Guangxing Wu, Runze Zhu, Yanqing Lu, et al

Opto-Electronic Science 2024, **3**(3): 230041 doi: 10.29026/oes.2024.230041

More related articles in Opto-Electronic Journals Group website

Opto-Electronic Journals Group

https://www.oejournal.org

OE_Journal

@OptoElectronAdv

Opto-Electronic Science

Article

June 2026, Vol. 5, No. 6

Open Access

Breaking the speed-resolution trade-off in 3.3-km non-line-of-sight imaging using scanning-free laser reflective tomography

Zewei Wang[1,2,3†], Xiaoyin Li[1,2†], Yinghui Guo[1,2,3,4*], Hengshuo Guo[5], Peng Yang[1,2,3], Fei Zhang[1,2,3], Mingbo Pu[1,2,3*], Mingfeng Xu[1,2,3] and Xiangang Luo[1,2,3*]

Abstract: Non-line-of-sight (NLOS) imaging, which allows the recovery of hidden scenes outside the direct view, holds immense potential across numerous fields. However, conventional scanning-based NLOS imaging systems, face a fundamental trade-off between imaging speed and resolution due to their reliance on scanning relay surfaces, where dense sampling prolongs measurement. Here, we introduce a scanning-free NLOS imaging technique that adapts laser reflective tomography (LRT) to reconstruct hidden objects by exploiting the diffuse relay surface as a natural beam expander. Our method requires only single-point detection of third-bounce photons, effectively breaking through the resolution and speed limitations imposed by scanning. Compared with scanning-based approaches, it delivers a twofold enhancement in spatial resolution and a 91-fold improvement in imaging speed. Furthermore, we extend the advantages of this method to long-range experiments, demonstrating NLOS imaging over 3.3 km with a resolution of 3 cm in 3 minutes, establishing new benchmarks in imaging range, resolution, and speed for NLOS imaging.

Keywords: non-line-of-sight imaging; laser reflective tomography; computational imaging

DOI: 10.29026/oes.2026.260007 | CSTR: 32246.14.oes.2026.260007

Citation: Wang ZW, Li XY, Guo YH et al. Breaking the speed-resolution trade-off in 3.3-km non-line-of-sight imaging using scanning-free laser reflective tomography. *Opto-Electron Sci* **5**, 260007 (2026).

1 Introduction

As a cutting-edge computational imaging technology capable of detecting hidden targets beyond direct visibility, non-line-of-sight (NLOS) imaging has garnered extensive attention in recent years[1]. By overcoming the inherent line-of-sight limitations of conventional imaging techniques, NLOS imaging holds significant potential across a wide range of domains including medical diagnosis, self-driving system, emergency search and rescue, and industrial inspection, providing innovative solutions to imaging challenges in complex scenarios. Over the past decades, diverse NLOS imaging approaches have been developed, including speckle correlation[2–6], wavefront shaping[7,8], neural network[9–11], and time-of-flight (ToF) imaging[12–15]. Some technologies have also confirmed that light field modulation methods exert an optimizing effect on NLOS imaging[8,16,17]. Among these, the ToF-based NLOS imaging has emerged as one of the most extensively explored methods attributed to its strong robustness against environmental interference and relatively mature technical framework.

Despite advances in hardware and reconstruction algorithms that have extended imaging range[18], enhanced resolution[19–21], and improved real-time performance[22–25], the ToF-based NLOS imaging systems remain fundamentally constrained by a trade-off between imaging speed and spatial resolution. In principle, these systems rely on scanning a relay surface with a pulsed laser, measuring the ToF signals of multiply scattered photons with high temporal resolution detectors, and then reconstructing the hidden scene through efficient algorithms. This scanning-based paradigm essentially leads to a conflict between achieving

Received: 5 February 2026

Accepted: 21 April 2026

Published online: 9 May 2026

[1]State Key Laboratory of Optical Field Manipulation Science and Technology, Institute of Optics and Electronics, Chinese Academy of Sciences, Chengdu 610209, China; [2]Research Center on Vector Optical Fields, Institute of Optics and Electronics, Chinese Academy of Sciences, Chengdu 610209, China; [3]College of Materials Sciences and Opto-Electronic Technology, University of Chinese Academy of Sciences, Beijing 100049, China; [4]Sichuan Provincial Engineering Research Center of Digital Materials, Chengdu 610299, China; [5]Tianfu Xinglong Lake Laboratory, Chengdu 610299, China.

[†]These authors contributed equally to this work.

*Correspondence: YH Guo, E-mail:gyh@ioe.ac.cn; MB Pu, E-mail: pmb@ioe.ac.cn; XG Luo, E-mail: lxg@ioe.ac.cn

fast imaging and high-resolution simultaneously. Achieving fast imaging requires decreasing the sampling density on the relay surface or shortening the acquisition time of each detection point, which leads to information loss or lower signal-to-noise ratio (SNR), thus degrading the image resolution. Some algorithms can mitigate the impact of under-sampling, but at the cost of increased reconstruction time[25–28]. While array detectors can acquire data rapidly, they face challenges in achieving high-resolution imaging due to high temporal jitter and photon crosstalk[23,24]. To achieve high-resolution imaging, a large-area dense scan of the relay surface is required to obtain sufficient spatial information, as the resolution improvement in NLOS imaging is closely related to the increase in scanning aperture. Usually, during the sampling process, the scanning area needs to at least exceed the orthographic projection area of the hidden scene. For example, detecting a hidden space of 40 cm × 40 cm × 40 cm requires a scanning aperture of at least 40 cm × 40 cm, but the resolution may still be insufficient to present the fine features of the hidden target at this time. To obtain higher resolution, the scanning aperture needs to be expanded several times, creating a contradiction where the smaller the hidden target, the larger the required scanning aperture. In addition, when the scanning aperture increases, the spacing between scanning points needs to be maintained smaller than the object detail size, which leads to an increase in the number of measurements and thus prolongs the overall acquisition process. At the same time, the expansion of the scanning aperture requires a large-area relay surface, which is difficult to achieve in practical applications. Therefore, if fast and high-resolution NLOS imaging can be achieved without scanning, using only a single relay point for detection, it will broaden the application potential of NLOS imaging.

In recent years, some breakthrough technologies in conventional line-of-sight imaging have achieved remarkable results in high-resolution and fast imaging[29–40], inspiring us to explore their application in NLOS scenarios to solve the above problems. Among them, laser reflective tomography (LRT) stands out as a non-scanning active imaging technique that can circumvent the resolution limitation imposed by aperture size[41–47]. Its basic principle is similar to that of computed tomography (CT), except that it uses reflection signals instead of transmission signals to reconstruct the object image. The specific process of LRT is to emit an extended laser pulse to completely cover the detection target, after a relative angular displacement occurs with the target and the laser echoes reflected by the target at different angles are received, then a tomographic algorithm is used for image reconstruction. The spatial resolution of this technology is primarily governed by the detector bandwidth, the laser pulse duration, and noise level, rather than the working distance or optical receiving aperture. As a result, LRT combines high-resolution with rapid acquisition, eliminating the need for point-by-point scanning.

Here, we present a novel NLOS imaging technique that adapts LRT to hidden scene reconstruction. By exploiting the diffuse scattering of a relay surface as a natural beam expander, we extend LRT principles to the NLOS regime, offering a novel imaging paradigm for scenarios such as detecting occluded rotating blades in engines or identifying vehicles or drones turning around corners. In short-range indoor experiments, our method reconstructs hidden objects using only triple-scattered light signals from a single point on the relay surface, delivering a 2-fold improvement in resolution and a 91-fold increase in imaging speed compared to conventional scanning-based NLOS imaging. Importantly, these advantages persist in long-range scenarios, where NLOS imaging is demonstrated at a distance of 3.3 km, attaining 3 cm resolution while requiring only 3 minutes for data collection, representing the longest-range NLOS imaging with the highest resolution and fastest speed reported to date.

2 Results

2.1 Principle of LRT for NLOS imaging

In typical ToF imaging NLOS systems, the main components are a laser, a time-resolved detector, a relay surface, and the hidden object. During imaging, short laser pulses illuminate the relay surface, then the light propagates into the occluded region, scatters from the hidden object, and returns to the relay surface for a third scattering before being captured by the detector. At the second scattering, the spatial features of the hidden object are encoded into the ToF of the scattered light. The detected signals can be processed using efficient algorithms to estimate the geometry of the concealed object. However, detecting only the signals from a single point on the relay surface is generally insufficient for NLOS image reconstruction. High-quality reconstruction requires dense scanning of the relay surface to acquire abundant data, which is time-consuming. Even with the use of array detectors or optimized algorithms to enhance data acquisition efficiency, another core limitation cannot be avoided: the requirement of a large scanning aperture for high-resolution imaging.

For the aforementioned NLOS imaging system, when it adopts a confocal configuration, i.e., the laser illumination point coincides with the detection point, the lateral resolution can be formulated as[12]:

$$\Delta x_s = \sqrt{1+\frac{z^2}{w^2}}\cdot\frac{c\gamma}{2}\ , \tag{1}$$

where z denotes the separation between the hidden object and the relay surface, w indicates the half-width of the scanning aperture, c represents the speed of light, and γ is the timing jitter associated with the detection system. Eq. (1) indicates that high-resolution imaging requires reducing z and γ, or increasing w. In practice, z cannot be actively controlled in NLOS scenarios, reducing γ is possible but often leads to increased system cost and complexity. Therefore, increasing w, that is, expanding the scanning aperture, represents the straightforward approach to enhance resolution. This principle aligns with conventional optical imaging systems, where larger aperture yields higher resolution. Nevertheless, in many real-world situations, the scanning aperture is constrained by the finite size of the relay surface, imposing a fundamental physical limit on the achievable resolution.

The imaging resolution of LRT is independent of the working distance and optical aperture, relying instead on the temporal resolution and SNR of the detection system. This property has already enabled LRT to overcome the aperture-limited lateral resolution in line-of-sight imaging, and it can likewise be harnessed to break the resolution constraint imposed by the scanning aperture in NLOS imaging. A key requirement for LRT is the use of a beam expander to expand the laser, enabling it to uniformly illuminate the entire target, ensuring complete information capture for reconstruction. Remarkably, this process bears a striking similarity to the propagation of light after its first scattering at the relay surface in NLOS imaging: the divergent scattered light naturally covers the hidden object, while in a confocal configuration, photons scattered from different parts of the object can be detected at the original illumination point on the relay surface. Owing to its ability to scatter light divergently into the hidden space, the relay surface can be regarded as a natural beam expander. This analogy provides a conceptual bridge for extending the LRT model to NLOS imaging, offering a pathway to transcend the resolution limitation.

The architecture of the NLOS imaging system based on LRT, as shown in Fig. 1(a), is basically consistent with the ToF-based configuration, with the primary distinction that it eliminates the need for scanning. In scenarios such as detecting rotating turbine blades in aero-engines or identifying vehicles or drones turning around corners, the hidden object undergoes rotation, leading to relative angular displacements between the object and the detection point.

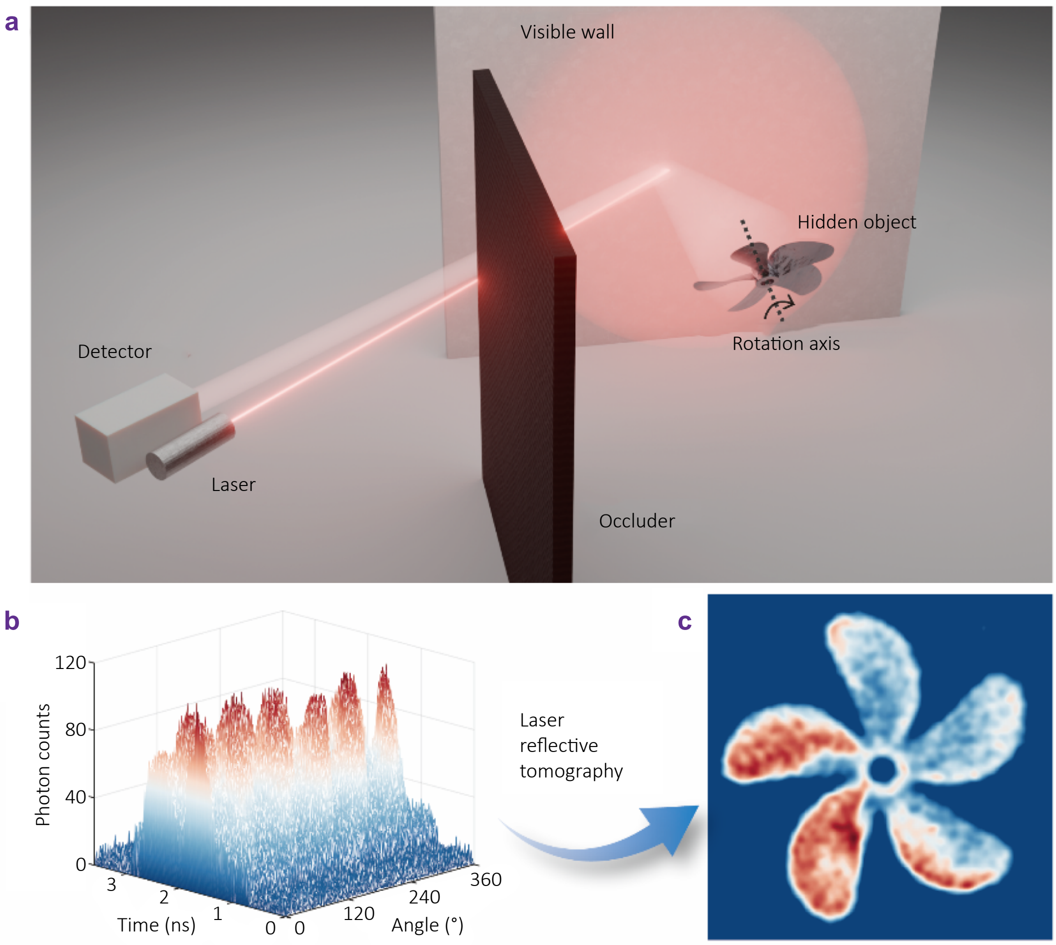

Fig. 1 | Schematic of LRT-based NLOS imaging. (a) Schematic diagram of imaging system architecture. (b) Angle-time data collected by LRT method. (c) The NLOS image reconstructed by tomographic algorithm.

The detector thus receives echo signals from the target at varying angles, which can be processed through tomographic imaging algorithms to reconstruct the hidden object.

In most practical situations, the hidden target is positioned far enough from the relay surface that the scattered light covering the object can be approximated as a parallel beam, thereby simplifying the LRT model in NLOS scenarios. To satisfy this approximation, the difference between the distances from the hidden object's edge and its center to the detection point should be smaller than the depth resolution of the imaging system:

$$\sqrt{\left(\frac{w_o}{2}\right)^2+z^2}-z\leq\frac{c\gamma}{2}\ , \tag{2}$$

where w_o is the width of the object. Specifically, the ray propagating along the parallel beam and the object's rotation axis intersect to define a plane, which we refer to as the meridional plane. The plane perpendicular to the meridional plane is defined as the sagittal plane. The projection of the hidden target's contour onto the sagittal plane can then be represented as a reflectivity function $f(x,y)$. At a given detection angle θ, the single-pixel detector records a one-dimensional triple-scattered signal modulated by the object, which is mathematically the Radon transform of partial $f(x,y)$ at this angle and can be described by:

$$p(r,\theta)=\int_{L_{r,\theta}}\frac{1}{r^4}f_1(x,y)\mathrm{d}l\ , \tag{3}$$

where $L_{r,\theta}$ denotes the ray along the propagation direction of the scattered light, $r=ct/2$ with c being the speed of light and t the ToF of the scattered photons, and $f_1(x,y)$ represents the portion of $f(x,y)$ facing the detection point. In LRT, light cannot penetrate the object, thus, the opposite region which is denoted as $f_2(x,y)$ cannot be measured. However, this complementary region contributes to the signal after the object rotates by π, yielding $p(r,\theta+\pi)$. By applying a symmetry transformation along the rotation axis, this signal is converted to:

$$p(2d-r,\theta+\pi)=\int_{L_{r,\theta}}\frac{1}{r^4}f_2(x,y)\mathrm{d}l\ , \tag{4}$$

where d is the perpendicular distance from the detection point to the object's rotation axis. Superimposing this transformed signal with the initial signal $p(r,\theta)$ provides the complete projection of the reflectivity function:

$$p^*(r,\theta)=p(r,\theta)+p(2d-r,\theta+\pi)=\int_{L_{r,\theta}}\frac{1}{r^4}f(x,y)\mathrm{d}l\ . \tag{5}$$

For a full rotation cycle of the object, if scattered signals are acquired at $2m$ angles, the superposition approach described above can be used to obtain complete projections at m angles, as illustrated in Fig. 1(b). The object's image can then be reconstructed using the filtered back-projection (FBP), a standard method in CT, with the reconstruction process described by:

$$f(x,y)=\sum_{i=1}^{m}F^{-1}\left\{|\omega|F\left[r^4p^*(r,\theta)\right]\right\}\ , \tag{6}$$

where $|\omega|$ is the frequency domain filter, F represents the Fourier transform, and F^{-1} denotes the inverse Fourier transform. The representative reconstruction outcome is shown in Fig. 1(c). In practice, this procedure involves applying Fourier transform to the projections from each angle, filtering in the frequency domain, combining the filtered data, and ending with an inverse Fourier transform to obtain the reconstructed image. More derivation details are provided in Supplementary Section 1.

By incorporating the above LRT workflow into an NLOS imaging scheme, the transverse resolution can be written as:

$$\Delta x_1=\frac{c\gamma}{2\cos\varphi}\ , \tag{7}$$

where φ represents the angle between the object surface and the sagittal plane. While this resolution is also influenced by the SNR of detection system in practice, it is no longer constrained by the separation between the target and the relay surface, nor by the scanning aperture. In scenarios where the object lies far from the relay surface or the detectable aperture on the relay surface is small, the condition $1/\cos\varphi<\sqrt{1+z^2/w^2}$ is generally satisfied. A comparison between Eq. (1) and Eq. (7) therefore indicates that LRT enables higher resolution in NLOS imaging.

Owing to its distinctive angular projection sampling scheme, LRT further enables substantially faster data acquisition. Whereas conventional scanning-based methods typically require tens of thousands of sampling points to achieve high-resolution reconstruction, LRT attains comparable or even higher resolution with data collected from only a few hundred angular projections. This markedly accelerates the imaging process and, importantly, requires only a single relay point for signal detection, thereby relaxing the constraints imposed on the relay surface.

2.2 Laboratory experiments

To validate the feasibility of NLOS imaging using LRT and compare its performance with conventional scanning-based approaches, we construct a confocal imaging system as presented in Fig. 2(a). The system employs a 1550-nm pulsed laser operating at 50 mW average power with a 12 MHz repetition rate and a 2 ps pulse width. A single-photon avalanche diode (SPAD) with a temporal jitter of ~80 ps is used in gating mode to detect scattered light signals, which gate out the signals of first-bounce light. A time-correlated single-photon counting (TCSPC) module with a temporal resolution of 1 ps records photon histograms at a temporal bin width of 16 ps. The overall system temporal jitter is ~100 ps, corresponding to a ranging resolution of 1.5 cm.

The experimental setup is installed in a laboratory

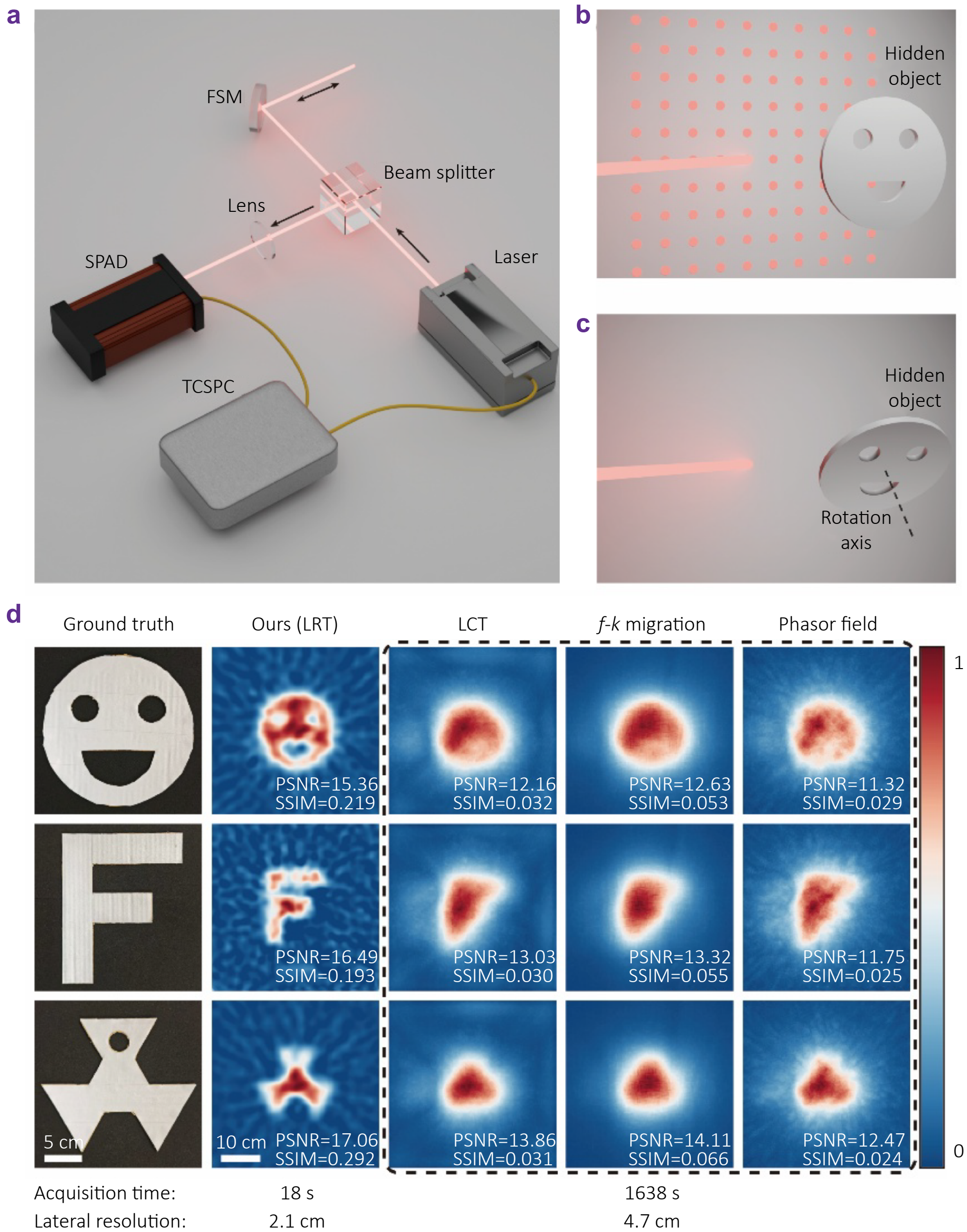

Fig. 2 | Experiments on short-range NLOS imaging based on LRT. (a) Diagram of the system optical path. (b) Schematic diagram of the point scanning mode. (c) Schematic diagram of the LRT mode. (d) Imaging targets and reconstruction results of different methods.

environment, where the laser is positioned about 5 m from the relay wall and illuminates the wall at an incident angle of ~45°. A photograph of the setup is provided in Supplementary Section 3. For scanning-based NLOS imaging, the hidden object is arranged to face the relay wall with a separation of 60 cm, as depicted in Fig. 2(b). A fast steering mirror (FSM) is used to deflect the laser, scanning a 43 cm × 43 cm area on the relay wall with 128 × 128 pixels. Each pixel has an exposure time of 0.1 s, leading to an overall acquisition time of ~1638 s. For LRT imaging, the hidden object is mounted on a rotation stage tilted at 45° relative to the horizontal plane and placed at the same 60 cm distance from the relay wall, as shown in Fig. 2(c). The FSM is fixed at the origin, such that only a single point on the relay wall is illuminated and detected, while the rotation stage is controlled to rotate at 20°/s. With data integrated every 0.1 s, a total of 180 angular views are acquired in 18 s for image reconstruction, giving LRT an acquisition rate 91 times higher than that of scanning-based imaging. The number of pixels in LRT reconstruction depends on the number of time bins recorded by the TCSPC, which can exceed tens of thousands, allowing for high-resolution reconstruction. For consistent comparison with scanning-based imaging, a 128 × 128 pixel region corresponding to a 43 cm^2 spatial area is selected from the reconstructed images.

Three different objects are reconstructed in experiments: a mask representing a human face, a letter "F" and a fan with a small hole on one of its vanes, as shown in Fig. 2(d). The two holes representing the eyes on the mask have a diameter of 4 cm, the parallel strokes of the "F" are spaced 4 cm apart, and the defect hole on the fan measures 3 cm in diameter. For the scanning-based data, reconstructions are performed using three fast imaging algorithms: LCT, *f-k* migration and phasor-field, each requiring tens of seconds for computation. In contrast, LRT reconstructions are performed using FBP, a fundamental and rapid CT algorithm which complete the computation in a few seconds.

The reconstruction results for each method are presented in Fig. 2(d). While scanning-based methods fail to resolve fine details of the objects, LRT clearly render these features. This outcome is consistent with the calculated lateral resolution of 4.7 cm for scanning-based imaging versus 2.1 cm for LRT, indicating a 2-fold improvement in resolution that matches the object feature scales. The quantitative evaluation of image quality is characterized by peak signal-to-noise ratio (PSNR) and structural similarity index (SSIM), both of which validate the superior performance of LRT, indicating smaller deviations from the ideal target and more complete structural recovery. The detailed parameters of the LRT reconstruction algorithm are described in Supplementary Section 2.

The LRT method is further extended to image a three-dimensional (3D) hidden object, a human head sculpture. In this experiment, the rotation stage is placed horizontally, with its rotation axis perpendicular to the horizontal plane, while other parameters remain identical to those used in the two-dimensional object imaging experiments. The target is rotated in three different poses, yielding three distinct projection views, as shown in Fig. 3. Using only a single relay point, LRT reconstructs 3D object as slice projections on the sagittal plane. Owing to the vertical rotation axis, the lateral resolution is improved to 1.5 cm, enabling clear reconstruction of the target's external contour.

2.3 Outfield experiments

The advantages of high-resolution and rapid imaging offered by LRT become more pronounced in long-range NLOS imaging. In distant scenarios, scattered photons are severely attenuated, necessitating increased exposure time to accumulate detectable signals. For scanning-based approaches, this requirement leads to prohibitively long acquisition time. In addition, the spatiotemporal broadening effect becomes more significant, further degrading resolution.

To assess the long-range NLOS imaging performance of LRT, outdoor experiments are conducted in the suburb of Chengdu. A satellite view of the experimental site is shown in Fig. 4(a). The imaging system is deployed at site A (30°26'39"N, 104°10'21"E), with a free-space link of 3.3 km to site B (30°25'22"N, 104°8'54"E), where the hidden scene is located. The optical layout is basically identical to the laboratory configuration, except for the addition of a custom telescope with a 350 mm aperture after the FSM to collimate the emitted laser and enhance the efficiency of collecting scattered light, and a narrowband filter to suppress interference from ambient light [Fig. 4(b)]. To ensure sufficient photon flux, a 1550-nm pulsed laser with 300 mW average power, 21 MHz repetition rate, and 7 ps pulse width is employed while retaining the same SPAD and TCSPC as in the laboratory experiments. The hidden scene is situated inside an observatory [Fig. 4(c)], where only a 0.5 m × 0.5 m diffuse relay wall is directly visible to the imaging system, and the hidden object is concealed behind a black curtain

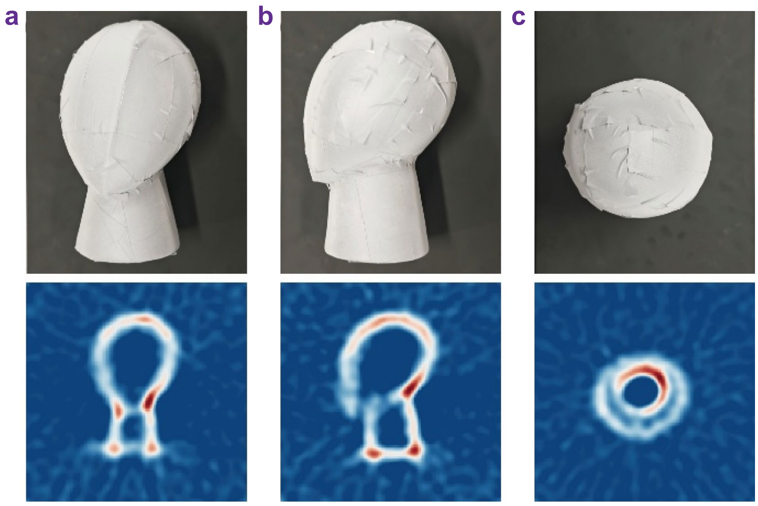

Fig. 3 | LRT reconstruction of NLOS 3D target. (a) View from the front. (b) View from the side. (c) View from the top.

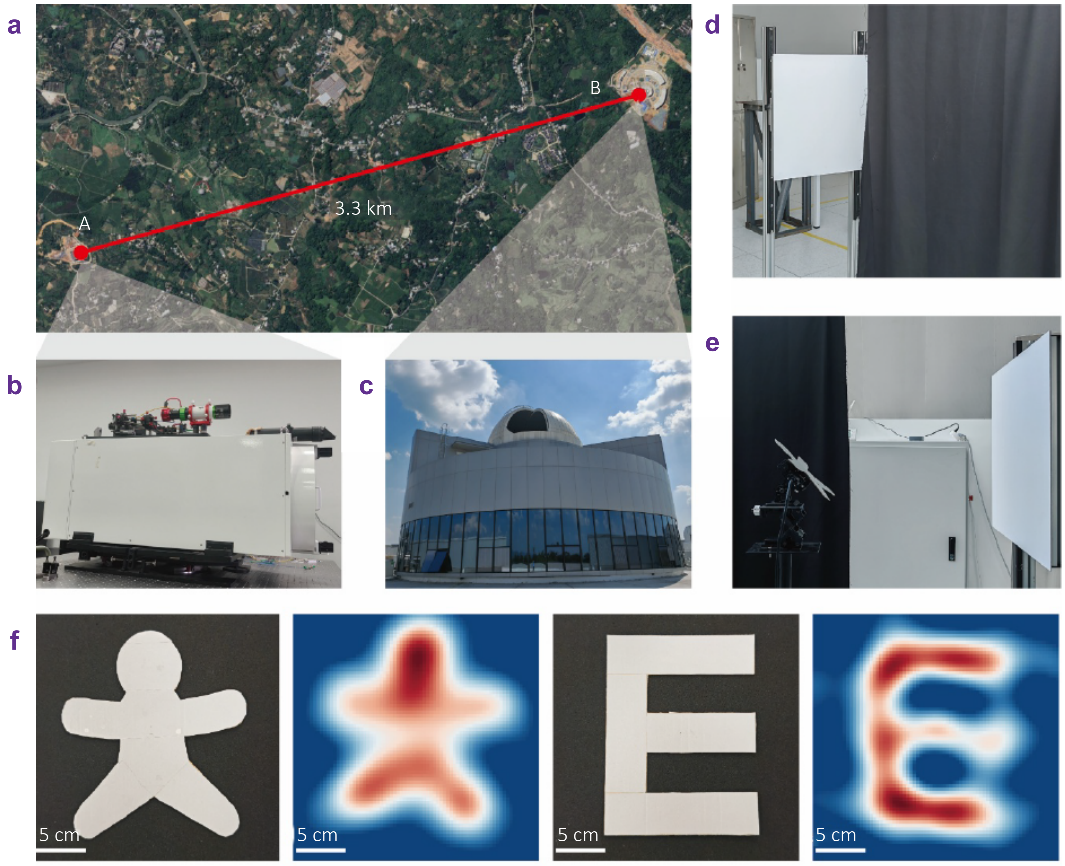

Fig. 4 | Experiments on long-range NLOS imaging based on LRT. (a) Satellite view of the experimental site. (b) Photograph of the detection system. (c) External view of the target end. (d) Scene within the field of view at the target end. (e) NLOS scene at the target end. (f) Imaging targets and their LRT reconstruction results.

[Fig. 4(d)]. The hidden object is mounted on a rotation stage tilted at 45° relative to the horizontal plane and placed ~60 cm from the relay wall [Fig. 4(e)]. The stage rotates at 2 °/s, and the imaging system integrates scattered light signals once per second, collecting data from 180 angular viewpoints over a total duration of 3 min. The system records data with a temporal bin width of 16 ps and a temporal jitter of ~200 ps. To suppress the spatiotemporal broadening effect and improve the signal intensity, the laser is focused onto the relay wall for illumination.

Figure 4(f) presents the reconstruction results using LRT for two different hidden objects, a humanoid model and a letter "E". The proposed method successfully generates clear images of both objects, achieving a resolution better than 3 cm, a level of performance unattainable with conventional scanning-based imaging. Figure 5 presents a comparison of our work with several other works, indicating that our work has the longest imaging range, relatively less acquisition time and higher resolution. Given that indoor experiments have already demonstrated the substantial advantages of LRT over scanning methods, and that a scanning approach

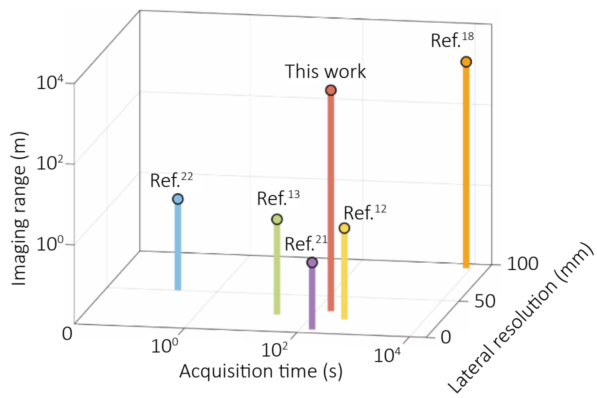

Fig. 5 | Comparison of performance metrics among different NLOS imaging works.

would have required a total acquisition time of ~4.5 h for this long-range scenario, rendering it significantly time-consuming and placing extreme demands on system stability and scanning precision, a long-range scanning-based NLOS imaging experiment is not performed.

3 Discussion

In summary, we introduce a rapid high-resolution NLOS imaging framework based on LRT. By exploiting diffuse relay surfaces as natural beam expanders, we demonstrate that the LRT model can be effectively applied to NLOS scenarios. Leveraging its aperture-independent resolution and unique angular projection acquisition mode, LRT overcomes the resolution and imaging speed limitations of conventional scanning-based approaches, achieving a 2-fold improvement in resolution and a 91-fold acceleration in imaging speed in laboratory experiments. We further extend the method to long-range applications, where it successfully reconstructs hidden objects at a distance of 3.3 km with a resolution better than 3 cm in only 3 min. To the best of our knowledge, this represents the highest resolution, fastest imaging speed, and longest detection range reported to date in the field of kilometer-scale NLOS imaging. This result indicates that the proposed LRT-based NLOS imaging is not limited to laboratory conditions but can evolve into a general tomographic sensing framework for dynamic industrial inspection, intelligent navigation, and remote sensing, laying the foundation for practical applications of NLOS imaging. Looking forward, for targets with non-uniform rotation or translational motion, motion estimation can be introduced to track the target, followed by motion-compensated reconstruction. Compressed sensing methods or reconstruction approaches incorporating prior information and regularization can be adopted to handle sparse and non-uniform sampling data. In addition, deep learning methods may also be applied to address complex motion scenarios. In this work, image reconstruction is performed using only the computationally efficient FBP algorithm to verify the feasibility of the proposed method. Iterative algorithms combined with total variation regularization can be adopted to improve the robustness of the reconstruction under low SNR conditions.

References

1. Faccio D, Velten A, Wetzstein G. Non-line-of-sight imaging. *Nat Rev Phys* **2**, 318–327 (2020).
2. Saunders C, Murray-Bruce J, Goyal VK. Computational periscopy with an ordinary digital camera. *Nature* **565**, 472–475 (2019).
3. Metzler CA, Heide F, Rangarajan P et al. Deep-inverse correlography: towards real-time high-resolution non-line-of-sight imaging. *Optica* **7**, 63–71 (2020).
4. Willomitzer F, Rangarajan PV, Li FQ et al. Fast non-line-of-sight imaging with high-resolution and wide field of view using synthetic wavelength holography. *Nat Commun* **12**, 6647 (2021).
5. Geng RX, Hu Y, Lu Z et al. Passive non-line-of-sight imaging using optimal transport. *IEEE Trans Image Process* **31**, 110–124 (2022).
6. Liu LF, Zhu S, Zhang WJ et al. Single-shot non-line-of-sight imaging based on chromato-axial differential correlography. *Photonics Res* **12**, 106–114 (2024).
7. Cao RZ, de Goumoens F, Blochet B et al. High-resolution non-line-of-sight imaging employing active focusing. *Nat Photonics* **16**, 462–468 (2022).
8. Guo YH, Lei YS, Pu MB et al. Vectorial digitelligent optics for high-resolution non-line-of-sight imaging. *Engineering* **45**, 70–78 (2025).
9. Shen SY, Wang Z, Liu P et al. Non-line-of-sight imaging via neural transient fields. *IEEE Trans Pattern Anal Mach Intell* **43**, 2257–2268 (2021).
10. Zhu DY, Cai WS. Fast non-line-of-sight imaging with two-step deep remapping. *ACS Photonics* **9**, 2046–2055 (2022).
11. He JH, Wu SK, Wei R et al. Non-line-of-sight imaging and tracking of moving objects based on deep learning. *Opt Express* **30**, 16758–16772 (2022).
12. O'Toole M, Lindell DB, Wetzstein G. Confocal non-line-of-sight imaging based on the light-cone transform. *Nature* **555**, 338–341 (2018).
13. Liu XC, Guillén I, La Manna M et al. Non-line-of-sight imaging using phasor-field virtual wave optics. *Nature* **572**, 620–623 (2019).
14. Lindell DB, Wetzstein G, O'Toole M. Wave-based non-line-of-sight imaging using fast *f-k* migration. *ACM Trans Graph* **38**, 116 (2019).
15. Feng XH, Gao L. Ultrafast light field tomography for snapshot transient and non-line-of-sight imaging. *Nat Commun* **12**, 2179 (2021).
16. Zhao ZB, Zhang Q, Li XY et al. High-resolution non-line-of-sight imaging based on liquid crystal planar optical elements. *Nanophotonics* **13**, 2161–2172 (2024).
17. Wang ZW, Li XY, Pu MB et al. Vectorial-optics-enabled multi-view non-line-of-sight imaging with high signal-to-noise ratio. *Laser Photon Rev* **18**, 2300909 (2024).
18. Wu C, Liu JJ, Huang X et al. Non-line-of-sight imaging over 1.43 km. *Proc Natl Acad Sci USA* **118**, e2024468118 (2021).
19. Wang B, Zheng MY, Han JJ et al. Non-line-of-sight imaging with picosecond temporal resolution. *Phys Rev Lett* **127**, 053602 (2021).
20. Liu XT, Wang JY, Li ZP et al. Non-line-of-sight reconstruction with signal-object collaborative regularization. *Light Sci Appl* **10**, 198 (2021).
21. Huang X, Ye RL, Li WW et al. Non-line-of-sight imaging and vibrometry using a comb-calibrated coherent sensor. *Phys Rev Lett* **132**, 233802 (2024).
22. Nam JH, Brandt E, Bauer S et al. Low-latency time-of-flight non-line-of-sight imaging at 5 frames per second. *Nat Commun* **12**, 6526 (2021).
23. Pei CQ, Zhang AK, Deng Y et al. Dynamic non-line-of-sight imaging system based on the optimization of point spread functions. *Opt Express* **29**, 32349–32364 (2021).
24. Zhang WJ, Guo EL, Zhu S et al. Real-time scan-free non-line-of-sight imaging. *APL Photonics* **9**, 126101 (2024).
25. Ye JT, Sun Y, Li WW et al. Real-time non-line-of-sight computational imaging using spectrum filtering and motion compensation. *Nat Comput Sci* **4**, 920–927 (2024).
26. Ye JT, Huang X, Li ZP et al. Compressed sensing for active non-line-of-sight imaging. *Opt Express* **29**, 1749–1763 (2021).
27. Liu XT, Wang JY, Xiao LP et al. Non-line-of-sight imaging with arbitrary illumination and detection pattern. *Nat Commun* **14**, 3230 (2023).
28. Ding R, Ye JT, Gao QF et al. Curvature regularization for non-line-of-sight imaging from under-sampled data. *IEEE Trans Pattern Anal Mach Intell* **46**, 8474–8485 (2024).
29. Hu YH, Zhang XY, Xu SL et al. Research progress of laser reflective tomography techniques. *Chin J Lasers* **48**, 0401002 (2021).
30. Wu GX, Zhu RZ, Lu YQ et al. Optical scanning endoscope via a single multimode optical fiber. *Opto-Electron Sci* **3**, 230041 (2024).
31. Bie SH, Tong XX, Lv ZY et al. Using cyclic Hadamard masks for single-pixel quantum imaging under entangled photon illumination. *Sci Adv* **11**, eadw4799 (2025).
32. Li FJ, Zhang HY, Lu ZL et al. Unsupervised learning enabled label-free single-pixel imaging for resilient information transmission through unknown dynamic scattering media. *Opto-Electron Adv* **8**,

250013 (2025).
33. Zhang Q, Lu YR, Guo YH et al. 200 mm optical synthetic aperture imaging over 120 meters distance via macroscopic Fourier ptychography. *Opt Express* **32**, 44252–44264 (2024).
34. Chen WW, Liu YF, Feng SJ et al. Dual-frequency angular-multiplexed fringe projection profilometry with deep learning: breaking hardware limits for ultra-high-speed 3D imaging. *Opto-Electron Adv* **8**, 250021 (2025).
35. Zhou R, Guo YH, Zhang Q et al. TurbFPNet: neural far-field turbulent Fourier ptychography with a camera array. *Optica* **12**, 1068–1078 (2025).
36. Li XY, Huang YJ, Guo YH et al. Sub-diffraction limited single-photon LiDAR with optimized confocal super-oscillatory illumination. *Laser Photon Rev* **19**, 2401837 (2025).
37. Luo XG. Digital optics and optical intelligent agent. *Appl Phys Lett* **127**, 010501 (2025).
38. Guo YH, Pu MB, Li Y et al. Surpassing the diffraction limit in long-range laser engineering via cross-scale vectorial optical field manipulation: perspectives and outlooks. *Opto-Electron Adv* **8**, 250256 (2025).
39. Guo YH, Pu MB, Xu MF et al. Revolutionary optical imaging enabled by vectorial and flat optics. *Adv Mater Technol* **11**, e02338 (2026).
40. Zhang Q, Shang Y, Guo Y et al. Long - range horizontal - path Fourier ptychography: a 1.4 - km experimental demonstration[J]. *Laser Photon Rev*, e71231(2026).
41. Parker JK, Craig EB, Klick DI et al. Reflective tomography: images from range-resolved laser radar measurements. *Appl Opt* **27**, 2642–2643 (1988).
42. Knight FK, Klick D, Ryan-Howard DP et al. Laser radar reflective tomography utilizing a streak camera for precise range resolution. *Appl Opt* **28**, 2196–2198 (1989).
43. Matson CL, Mosley DE. Reflective tomography reconstruction of satellite features - field results. *Appl Opt* **40**, 2290–2296 (2001).
44. Wang JC, Zhou SW, Shi L et al. Image quality analysis and improvement of Ladar reflective tomography for space object recognition. *Opt Commun* **359**, 177–183 (2016).
45. Guo R, Jin ZH, Zhang WB et al. Lidar reflective tomography of the target under incomplete view state. *IEEE J Miniat Air Space Syst* **4**, 25–32 (2023).
46. Li ZP, Ye JT, Ye WL et al. Single-photon laser reflective tomography over 7 km. *Opt Lett* **50**, 2970–2973 (2025).
47. Zhang XY, Shan LQ, Fang JJ et al. Super-resolution imaging using reflective tomography LiDAR over 10 km. *Adv Imaging* **2**, 051002 (2025).

Acknowledgements

This work was supported by Temporal-spatial manipulation Infrastructure for vector Fields in Optics-Test Facility (TIFO-TF). We are grateful for financial supports from the National Key Research and Development Program of China (2023YFB2805800); National Natural Science Foundation of China (U24A6010, U25A20518); Sichuan Science and Technology Program (2021ZYCD001).

Author contributions

XG Luo supervised the project; YH Guo, MB Pu and XG Luo designed the research; ZW Wang, XY Li, YH Guo, P Yang, and HS Guo performed the research; ZW Wang, P Yang, HS Guo, F Zhang and MF Xu analyzed the data; ZW Wang, XY Li, YH Guo and MB Pu wrote the paper. All authors were closely involved in discussing and revising the manuscript.

Competing interests

Mingbo Pu and Xiangang Luo serve as Editors for the Journal, no other author has reported any competing interests.

Supplementary information

Supplementary information for this paper is available at https://doi.org/10.29026/oes.2026.260007

Open Access This article is licensed under a Creative Commons Attribution 4.0 International License, which permits use, sharing, adaptation, distribution and reproduction in any medium or format, as long as you give appropriate credit to the original author(s) and the source, provide a link to the Creative Commons license, and indicate if changes were made. To view a copy of this license, visit http://creativecommons.org/licenses/by/4.0/
©The Author(s) 2026.
Published by Editorial Office of *Opto-Electronic Science*, Institute of Optics and Electronics, Chinese Academy of Sciences.

Opto-Electronic Journals Group
www.oejournal.org
Scan for Article PDF